Fabrication and characterization of porous mullite ceramics derived from fluoride-assisted Metakaolin-Al(OH)$_3$ annealing for filtration applications

Amanmyrat Abdullayev [a], Celal Avcioglu [a], Tobias Fey [b,c], André Hilger [d], Markus Osenberg [d], Ingo Manke [d], Laura M. Henning [a], Aleksander Gurlo [a], Maged F. Bekheet [a,*]

[a] *Fachgebiet Keramische Werkstoffe / Chair of Advanced Ceramic Materials, Institute of Materials Science and Technology, Technische Universität Berlin, 10623, Berlin, Germany*
[b] *Department of Materials Science and Engineering, Institute of Glass and Ceramics, University of Erlangen-Nürnberg, Erlangen, Germany*
[c] *Frontier Research Institute for Materials Science, Nagoya Institute of Technology, Nagoya, Japan*
[d] *Institute of Applied Materials, Helmholtz Centre for Materials and Energy, Berlin, Germany*

A B S T R A C T

In this work, polycrystalline mullite whiskers are synthesized by fluoride-assisted method from metakaolin and several aluminum-containing compounds such as γ-Al(OH)$_3$, AlF$_3$·3H$_2$O, and α-Al$_2$O$_3$ (corundum). The mullite formation and crystallization are assessed both in ex situ and in situ synchrotron X-ray diffraction experiments under synthesis conditions. Polycrystalline mullite starts to form from metakaolin, Al(OH)$_3$, and AlF$_3$·3H$_2$O reactants at 680 °C, whereas mullite does not form even at 1000 °C when corundum is used. Porous mullite ceramics are fabricated at sintering temperatures between 1000 and 1700 °C and tested for water permeance. Scanning Electron Microscopy (SEM) and synchrotron X-ray tomography (μCT) reveal that ceramics are comprised of pore channels with an interlocked network of mullite whiskers. With competitive porosity (up to 63 %), compressive strength (up to 20 MPa), and pure water flux (up to 579 L/m^2·h at 1 bar), fabricated mullite ceramics are promising candidates for water filtration and purification.

1. Introduction

Water pollution, particularly contamination of clean water resources and inadequate wastewater treatment, poses a significant risk to public health and the ecosystem [1]. Hence, clean water and water sanitation became one of the 17 sustainable development goals of the United Nations (UN). One of the effective methods for wastewater treatment is the use of ceramic membranes [2]. Commercially available ceramic membranes are typically made from Al$_2$O$_3$, TiO$_2$, SiC, and ZrO$_2$ [3]. However, costly raw materials and high-temperature processing requirements prevent their large-scale implementation in wastewater treatment. Therefore, the fabrication of ceramic membranes from low-cost materials using relatively low-temperature manufacturing processes would minimize their ecological footprint and encourage widespread application, particularly in the Global South countries. In this direction, the past few decades have witnessed a dramatic growth of research interest in exploiting cost-effective ceramic membrane production methods [4,5].

Among various structural engineering materials, porous mullite (3Al$_2$O$_3$·2SiO$_2$) ceramics have attracted much attention regarding their outstanding merits, such as high mechanical strength, good stability in harsh conditions, good antifouling properties, thermal shock, creep, and pressure resistances [6]. Besides, various affordable minerals and industrial wastes, such as aluminum sludge, coal fly ash, rice husk silica, coal gangue, sago waste, topaz sand, diatomite, bauxite, ball clay, and kaolin, have been employed as starting materials for the production of mullite ceramics [5]. Nevertheless, its synthesis from clay minerals remains the most viable option in terms of cost-efficiency. For instance, mullite could be obtained by high-temperature treatment of kaolin, which is the most prominent member of the clay family and costs only 1 $/kg. Kaolin transforms first into metakaolin (eq. (1)) in the temperature range of 400–700 °C, before decomposing into crystalline mullite and silica (SiO$_2$) at temperatures above 1000 °C (eq. (2)) [7]. However, the formation of the residual silica phase along with mullite is detrimental to the thermochemical properties. Accordingly, an additional alumina source has been applied during the synthesis to react with the excess silica in metakaolin to produce phase pure mullite ceramics [7,8]. In this regard, pure corundum (α-Al$_2$O$_3$) is the most preferred additional alumina source due to its high purity [9]. However, difficulties arise in

---

Table 1
Chemical composition of metakaolin as determined by XRF.

Compound	Weight fraction, %	Molar fraction, %
SiO_2	53.75	66.35
Al_2O_3	43.82	31.82
Fe_2O_3	0.45	0.21
CaO	0.16	0.21
K_2O	0.18	0.14
Na_2O	0.26	0.31
SO_3	0.02	0.02
P_2O_5	0.43	0.14
TiO_2	0.86	0.79

reacting the excess silica when corundum (α-Al_2O_3) is mechanically mixed to form mullite, because this reaction requires relatively high temperatures (>1400 $^\circ$C). The formation temperature of mullite could be reduced to below 1400 $^\circ$C when liquid phase forming additives, e. g., TiO_2 [10], Y_2O_3 [11], Fe_2O_3 [12] were added during the synthesis process. Yet, even with the assistance of these additives, complete mullite formation from kaolin and corundum mixture requires temperatures higher than 1100 $^\circ$C. Besides, these liquid phase forming agents may form residual glassy silicate phases, adversely affecting mullite properties.

$$Al_2O_3 \cdot 2SiO_2 \cdot 2H_2O \xrightarrow{400-700 \ ^\circ C} Al_2O_3 \cdot 2SiO_2 + 2H_2O \qquad (1)$$

$$3(Al_2O_3 \cdot 2SiO_2) \xrightarrow{>1000 \ ^\circ C} 3Al_2O_3 \cdot 2SiO_2 + 4SiO_2 \qquad (2)$$
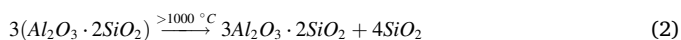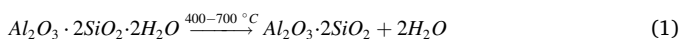
Recent studies have shown that gas-phase forming additives, such as AlF_3, are more beneficial than liquid phase forming agents to lower the mullitization temperature as well as obtain phase-pure mullite [9, 13–16]. The challenge to reduce the mullitization temperature lower than 1000 °C still remains when corundum is used. However, recently, a synthesis of phase-pure mullite was achieved at temperatures as low as 800 °C by utilizing $Al_2(SO_4)_3$ instead of corundum as an alumina source under the fluoride-assisted synthesis conditions [17]. But, since $Al_2(SO_4)_3$ decomposes to toxic sulfur oxides, this compound is not favorable for environmental reasons.

Accordingly, in the present work, we use natural mineral metakaolin as a primary raw material and either gibbsite (γ-$Al(OH)_3$) or corundum (α-Al_2O_3) as an additional aluminum source to synthesize mullite using the fluoride-assisted method. Although Chen et al. could synthesize mullite from natural mineral kaolin combined with additives $Al(OH)_3$ and AlF_3 as alumina sources above 1300 °C, the exact amounts of used alumina additives were not given in this work [18]. However, the formation of mullite from different clay materials and alumina sources might require a high amount of AlF_3 additive (i.e., 40 wt% of total powder mixture) [9]. Thus, in this work, guided by in situ synchrotron XRD experiments, we could successfully synthesize the mullite at much lower temperatures (~700 °C) using low content of AlF_3 that does not exceed 10 wt% of total powder. Moreover, the feasibility of porous mullite membrane support fabrication is investigated using a mixture of metakaolin, $Al(OH)_3$, and $AlF_3 \cdot 3H_2O$ powders. By altering annealing conditions, mullite ceramics with varying morphologies, pore sizes, and mechanical strengths are obtained, then their performances are systematically evaluated.

2. Materials and methods

2.1. Materials

Metakaolin (Metamax, BASF, hereafter denoted as MK), which is a calcined form of kaolin clay, was used as the main raw material. Aluminum hydroxide (γ-$Al(OH)_3$, >99%, Merck) corundum (α-Al_2O_3, 99.99%, AKP-50, Sumitomo), aluminum fluoride trihydrate ($AlF_3 \cdot 3H_2O$, $\geq$97%, Ventron) were used as an additional alumina source and

mineralizer, respectively.

2.2. The synthesis of mullite powders

Crystalline mullites were synthesized by fluoride-assisted solid-state route as described below. In order to ascertain the molar ratio of alumina to silica, the silica and alumina content of the clay (MK) was analyzed by XRF, revealing a ratio of 1:2 (Table 1). Thus, 13.7 g γ-Al $(OH)_3$ and 2.7 g $AlF_3 \cdot 3H_2O$ were added as additional alumina sources to 11.0 g MK to obtain the P-1 precursor for synthesizing $3Al_2O_3 \cdot 2SiO_2$ (3:2 mullite). To study the influence of aluminum source on the crystallization of mullite, a stoichiometric amount of α-Al_2O_3 was added instead of γ-$Al(OH)_3$ to $AlF_3 \cdot 3H_2O$ and MK to obtain the P-2 precursor. The powder mixtures were mixed in an agate mortar and pestle for 10 min before placing them in closed alumina crucibles. The crucibles were heated at 1000 $^\circ$C for 30 min (heating and cooling rates of 5 K min^{-1}) in a resistive furnace (Nabertherm).

2.3. The fabrication of porous mullite ceramics

Cylindrical samples with 6 mm diameter and 12 mm height were prepared for porosity, compressive strength, μCT, and mercury intrusion tests. Disc-shaped samples with 25 mm diameter and ~3 mm thickness were prepared for the water permeance test as follows. The M-1 powder mixture was first prepared from MK, $Al(OH)_3$, and $AlF_3 \cdot 3H_2O$, as described above. Then, 3.85 wt% of 5 wt% PVA solution were added to the powder mixtures as a binder for pressing. In the next step, the ground powder mixtures were pelletized at 50 MPa for 5 min by uniaxial compression (Paul-Otto Weber, Germany). After compression, the obtained green bodies were dried at 24 $^\circ$C for 24 h before heating them in covered alumina crucibles. Alumina paste was applied between the crucible and lid to minimize the escape of reactive gases from the system at high temperatures. Then the closed crucibles were heated first at 1000 $^\circ$C in a resistive furnace (Nabertherm) with a heating rate of 2.5 K min^{-1}, a holding time of 60 min, and a cooling rate of 5 K min^{-1} to obtain porous mullite bodies, this specimen is denoted as M-10. Subsequently, samples were sintered at several temperatures (1400 $^\circ$C, 1500 $^\circ$C, 1600 $^\circ$C, and 1700 $^\circ$C) with a heating rate of 5 K min^{-1}, holding time of 4 h and cooling rate of 5 K min^{-1}. For convenience, the obtained samples were denoted as M-14, M-15, M-16, and M-17 according to their sintering temperatures.

2.4. Characterizations

2.4.1. Powder X-ray diffraction

The ex situ powder X-ray diffraction (PXRD) measurements were performed at room temperature (RT) in a D8 Advance (Brucker, Germany) using CuK$_\alpha$ radiation in the 2θ range of 10–70° with a step size of 0.02° and step time of 8 s.

The in situ high-temperature synchrotron XRD experiments were performed at the beamline 12.2.2, Advanced Light Source (Lawrence Berkeley National Laboratory, California, USA) using monochromatic synchrotron radiation with λ = 0.495 Å (25 keV/30 mm spot size) in the angle-dispersive transmission mode using a Pilatus detector. About 1 mg of the powder sample was heated in a 0.7 mm outer diameter quartz capillary (Hilgenberg GmbH, Germany) under quasi-flowing conditions (O_2:N_2 = 1:4). The gases were injected through a 0.5 mm outer diameter tungsten tube. The capillary was heated at 20 K min^{-1} from RT to 950 $^\circ$C in an infrared heated SiC tube furnace as described elsewhere [19,20]. Diffraction patterns were recorded every 60 s during the heating cycle.

2.4.2. SEM

The microstructure of samples was investigated using Scanning Electron Microscopy (SEM) LEO 1530 (Carl Zeiss, Jena, Germany). The specimens for SEM characterization were cut from the middle of cylindrical samples using a diamond disc and then washed in an ultrasonic
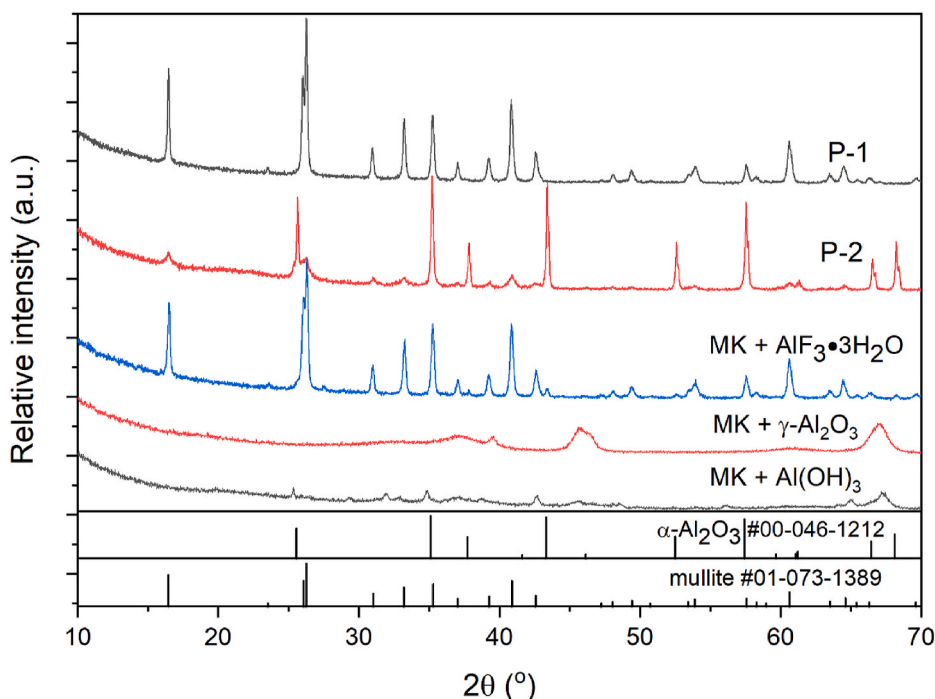
Fig. 1. XRD patterns of mullite prepared using different sources of additional aluminum to consume excess silica in metakaolin. P-1 is obtained from the mixture of metakaolin, γ-Al(OH)$_3$ and AlF$_3$·3H$_2$O; P-2 is obtained from the mixture of metakaolin, α-Al$_2$O$_3$ and AlF$_3$·3H$_2$O. Additionally, XRD patterns of metakaolin plus AlF$_3$·3H$_2$O, metakaolin plus γ-Al$_2$O$_3$, and metakaolin plus Al(OH)$_3$ are presented as controls, which prove that only P-1 precursor is capable of producing mullite at that at 1000 °C. Calculated patterns of α-Al$_2$O$_3$ and mullite are presented as a reference at the bottom of the image.

bath to remove the loose dust particles before sputtering with a carbon layer.

2.4.3. Synchrotron X-ray tomography (μCT)

Synchrotron X-ray tomography was carried out at the BAMline at BESSY II of Helmholtz-Centre Berlin, Germany. The synchrotron beam was monochromatized to 20 keV using a double multilayer monochromator with an energy resolution of about 1.5 %. The detector system is comprised a CdWO$_4$ scintillator, a microscopic optic, and a pco. edge camera with a 2560×2160 pixel^2 sCMOS chip. The pixel size was 0.72 μm, and the corresponding field of view was 1.8×1.6 mm^2 (length $\times$ height). For the tomographic reconstruction, an implementation of a filtered back-projection algorithm, the IDL-based library called "gridrec" was used [21].

The geodesic tortuosity is defined as a ratio of the lengths of the shortest transportation paths (geodesic lengths) to euclidean lengths. Tortuosities were calculated of a volume of $1500 \times 1500 \times 1500$ voxel using the geodesic distance transformation [22].

2.4.4. Porosity characterization

The open porosity of sintered mullite ceramics was determined by the Archimedes method, according to the ASTM C-373-18 [23] as follows. The dried samples were first weighed before the Archimedes experiments to determine W$_d$, and then the samples were submerged into the water until the open porosities were saturated with water. While the samples were in the water, their weights were recorded to determine the suspended weights (W$_s$). Subsequently, the samples were taken out from the water, and the surfaces were gently dried using a microfiber cloth, before weighing the samples to determine their saturated weights (W$_m$). The open porosity (φ) was calculated from dry (W$_d$), suspended (W$_s$) and saturated (W$_m$) weights according to Eq. (3).

$$\varphi = \frac{W_m - W_d}{W_m - W_s} * 100 \ (\%) \tag{3}$$

Pore size distribution was analyzed with a mercury intrusion porosimeter (Pascal 140, Porotec, Germany). It should be emphasized that the mercury porosimetry relies on the Washburn equation, which is applicable for cylindrical pores [24]. In this work, pores were assumed to be cylindrical, and the pore size distributions were presented for comparison purposes.

The diameter of disc-shaped samples before and after heat treatment was measured using a digital micrometer (Micromar 40 EWR, Mahr, Germany) with a precision of 0.001 mm. From the change in diameter of the samples, shrinkage was calculated according to Eq. (4):

$$\text{shrinkage} = \frac{d_0 - d_f}{d_0} * 100 \ (\%) \tag{4}$$

where d$_0$ and d$_f$ represent the diameter of samples before and after heat treatment, respectively.

2.4.5. Mechanical stability

The mechanical stability of sintered cylindrical mullite ceramics, i.e., 4.7–6.1 mm in diameter and 10–13 mm in height, was evaluated by compressive testing in a RetroLine testing machine using testXpert v.11 software (Zwick/Roell, Ulm, Germany). Briefly, cylindrical samples were compressed with a testing speed of 0.5 mm min^{-1} until fracture occurred or deformation exceeded 10%. The compressive strength was obtained from the quotient of maximum force and cross sectional area of the test piece. At least four replicas were tested for each sample.

2.4.6. Pure water permeance

A lab-built dead-end filtration setup was used for the water permeance tests as described elsewhere [25]. Briefly, the ceramic membrane support was first placed on the bottom of the stainless-steel container and fixed with O-rings to prevent leakage or bypass of water. Then, the container was filled with distilled water and pressurized with nitrogen gas; the volume of water passed through the membrane was recorded. Water flux was evaluated at different water pressures according to Eq. (5):

$$J_w = \frac{Q}{A\Delta t} \tag{5}$$

where J$_w$ is the water flux (L/m^2·h), Q is the volume of permeated water (L), A is the effective surface area of membrane (m^2), and Δt is the time spent for the permeation of water (h).
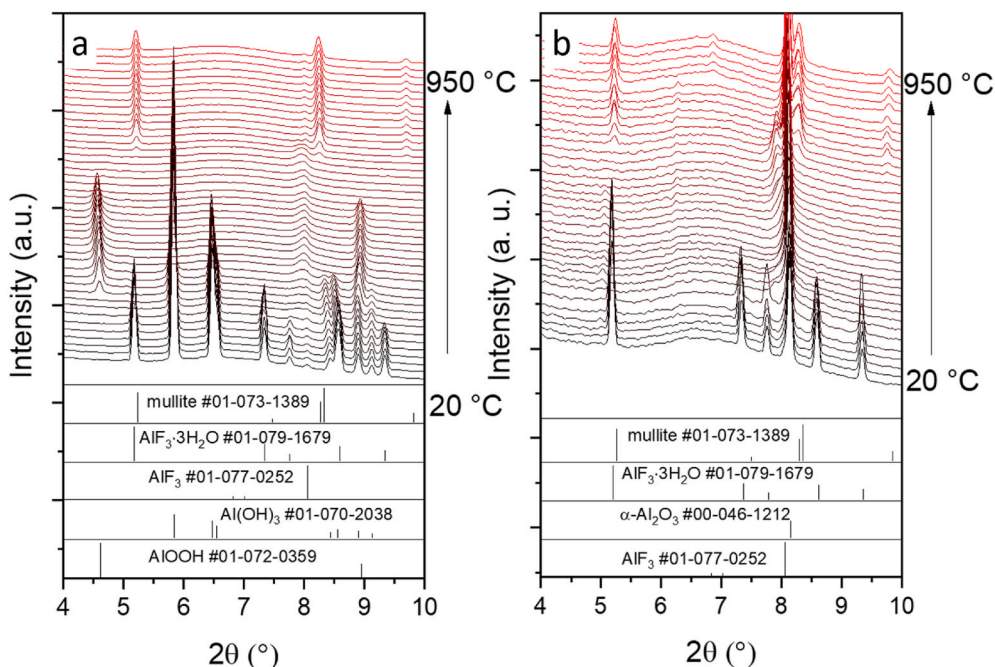
Fig. 2. In situ heating XRD patterns of precursor P-1 (a) and precursor P-2 (b) from room temperature to 950 °C. Calculated patterns of phases are presented at the bottom as reference.

3. Results and discussion

3.1. Synthesis conditions of polycrystalline mullite powders assisted by in situ synchrotron XRD experiments

Fig. 1 shows ex situ XRD patterns of the samples obtained by heating P-1 and P-2 precursors at 1000 °C. The heat treatment of the precursor P-1 results in the formation of phase-pure mullite, indicating the successful reaction between $Al(OH)_3$, AlF_3, and MK at 1000 °C. In contrast, when P-2 is used, the corundum (α-Al_2O_3) is still the primary phase, and only a small amount of mullite phase is formed, which is the product of the reaction of AlF_3 with silica [26]. This finding is also confirmed by reacting only MK and $AlF_3\cdot3H_2O$ with a weight ratio of 1:1, which leads to the formation of phase-pure mullite (Fig. 1). However, using such a high amount of $AlF_3\cdot3H_2O$ is neither environmentally nor economically feasible. These results suggest that α-Al_2O_3 does not react with MK at
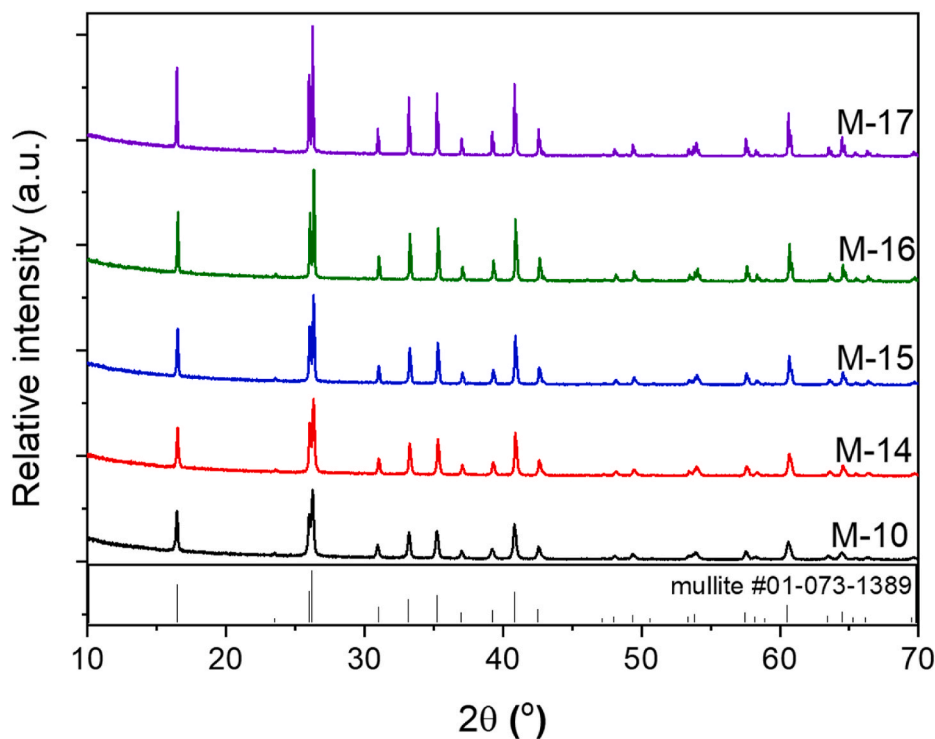

Fig. 3. XRD patterns of mullite prepared from the mixture of metakaolin, γ-$Al(OH)_3$ and $AlF_3\cdot3H_2O$ at 1000 °C and sintered at 1000 °C (M-10) followed by another sintering step at 1400 °C (M-14), 1500 °C (M-15), 1600 °C (M-16), and 1700 °C(M-17).
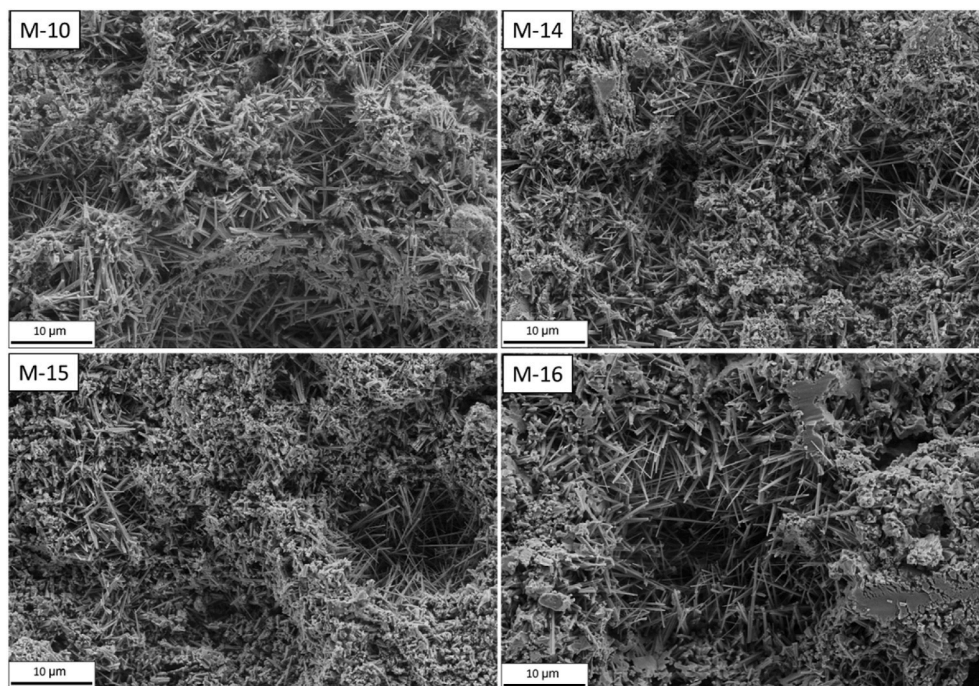
Fig. 4. SEM images of cross-section of porous mullite membranes consisting of an interlocked network of mullite whiskers. Samples were prepared at different sintering temperatures (M-10 at 1000 °C, M-14 at 1400 °C, M-15 at 1500 °C, and M-16 at 1600 °C).

these experimental conditions. Moreover, several other control experiments using different starting powder compositions, e.g. MK/Al(OH)$_3$ or MK/γ-Al$_2$O$_3$, shows that mullite can not be obtained under these circumstances without AlF$_3$, see Fig. 1. This finding is in agreement with the literature, which shows the importance of fluoride for the low-temperature formation of mullite [15–17]. It should be noted that not only fluoride is important in mullite formation, but also Al$_2$O$_3$ phase is also crucial. For instance, in our previous work, we observed that in the presence of AlF$_3$, mullite was formed only if Al$_2$(SO$_4$)$_3$ was used as an alumina source, while no mullite was formed when α-Al$_2$O$_3$ or γ-Al$_2$O$_3$ was used [17].

To get better insight into the formation mechanism of polycrystalline mullite, the transformation of precursors P-1 and P-2 into polycrystalline mullite was followed by in situ synchrotron XRD experiments during heating from room temperature up to 950 °C in air. Fig. 2 a and b display the in situ XRD patterns collected during the heating of both precursors under the air atmosphere. As shown in Fig. 2a, the precursor M-1 contains crystalline gibbsite Al(OH)$_3$ and AlF$_3$·3H$_2$O in addition to the amorphous MK phase.

The in situ XRD data reveal that the heating of the precursor P-1 leads to several consecutive changes with temperature. First, the AlF$_3$·3H$_2$O phase is transformed into anhydrous rhombohedral AlF$_3$ at 200 °C by losing its chemically bonded water, which is consistent with previous reports [17,27]. At 250 °C, gibbsite γ−Al(OH)$_3$ starts to transform into the boehmite γ−AlOOH phase. The later phase transformation continues until 330 °C, which agrees with previously reported works [28]. At 540 °C, the boehmite phase starts to transform into an amorphous alumina phase [28,29] that reacts with AlF$_3$ and amorphous MK at 685 °C to form mullite phase. Surprisingly, no fluorotopaz (Al$_2$SiO$_4$F$_2$) phase is observed in the in situ XRD experiments. Previous works reported that the fluorotopaz phase is formed from clay and Al$_2$O$_3$ in the presence of silicon tetrafluoride (SiF$_4$) gas under similar conditions at temperatures below 900 °C, before decomposing endothermically to form mullite and SiF$_4$ above 1100 °C [30–32]. The results of the in situ XRD experiments suggest that mullite can form directly from the mixture of MK, γ-Al(OH)$_3$, and AlF$_3$·3H$_2$O without forming fluorotopaz as an intermediate phase, which is in agreement with several recent

works [33,34].

For the precursor P-2, α-Al$_2$O$_3$ and AlF$_3$·3H$_2$O were found at room temperature in addition to the amorphous MK phase. Similar to the precursor P-1, AlF$_3$·3H$_2$O transforms into anhydrous AlF$_3$ at 200 °C before the formation of a small amount of mullite phase at 685 °C. However, the corundum α-Al$_2$O$_3$ phase was stable during the entire experiment, implying that corundum is not involved in the formation of the mullite phase. This small amount of mullite formed is due to the reaction between MK and AlF$_3$. These results are in good agreement with previous works that suggest temperatures higher than 1100 °C are required for the formation of mullite from corundum and silica phases [9,35,36].

3.2. The phase composition of mullite ceramics

The phase composition of mullite ceramics obtained by calcination and sintering of P-1 precursors at various temperatures was investigated using ex situ XRD characterization. As shown in Fig. 3, all samples contain only a polycrystalline mullite phase.

The XRD reflections become sharper and narrower with increasing the sintering temperatures, suggesting the increase in the crystallinity and crystallite size of the mullite phase. However, other than that, no significant microstructural change was observed, implying that obtained mullite does not undergo any considerable structural change even for high-temperature treatment at 1700 °C.

3.3. The microstructure of mullite ceramics

SEM images of the porous mullite ceramics, which were prepared at several different temperatures, are presented in Fig. 4. Under fluoride-assisted conditions, mullite forms in a solid-gas reaction, and due to fewer constraints, mullite crystals grow faster along the *c* direction [14]. Consequently, these mullite whiskers with various lengths produce a highly porous interlocked network of mullite, which is consistent with previous works [9,37,38].

Surprisingly, there is not much difference observed in the microstructure when increasing the sintering temperature from 1000 °C to
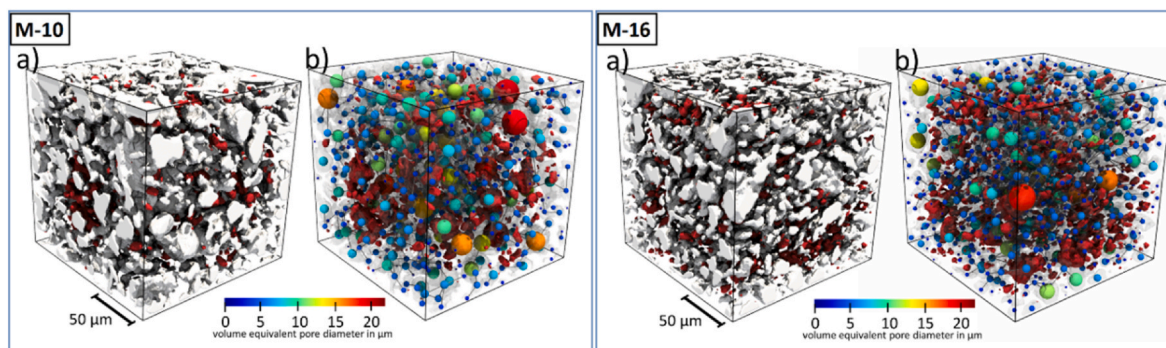
Fig. 5. Partial volumes of reconstructed µCT images for samples M-10 and M-16. a): The images show the network that contains nanopores. The main network was rendered with a white surface, while sections without connection to the outside were rendered in red. b): Here, the now transparent main network contains spheres with the pore equivalent diameter (colored accordingly). The spheres have been connected with each other based on the underlying network structure. (For interpretation of the references to color in this figure legend, the reader is referred to the Web version of this article.)
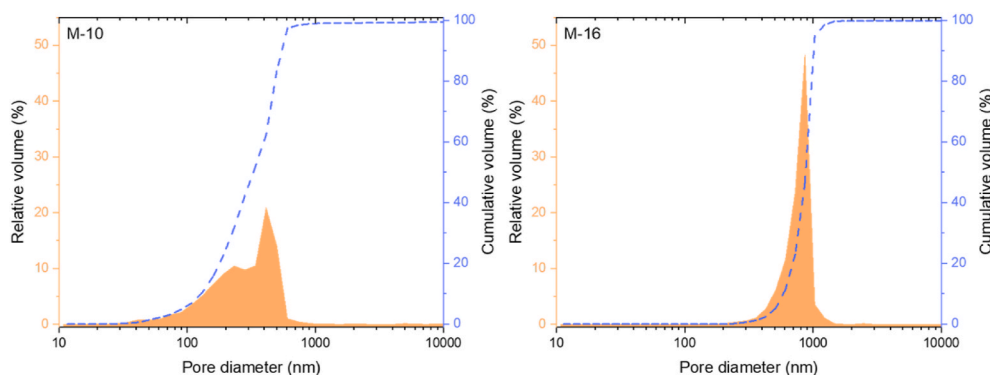

Fig. 6. Pore size distribution of samples M-10 and M-16.

1600 °C. Only at 1600 °C, better densification of porous mullite matrix can be seen, particularly on the wall or strut of pores, due to the increase in the sinterability of mullite at such a high temperature. This is also supported by porosity and shrinkage findings. Nevertheless, the nest-like structure of interlocked mullite whiskers network remains present in both samples.

µCT characterization also revealed that samples M-10 and M-16 display similar microstructure (Fig. 5). However, it should be noted that the pixel size of µCT equipment is 0.72 µm/voxel, which means smaller pores were not detectable with this technique. Nevertheless, the skeletonized images show that both samples exhibit a connected network of pores (see Fig. 5). Moreover, tortuosity of pores was calculated using reconstructed µCT tomograms, and it was found that M-10 and M-16 possess tortuosity factor of 1.21 and 1.29, respectively, being in this
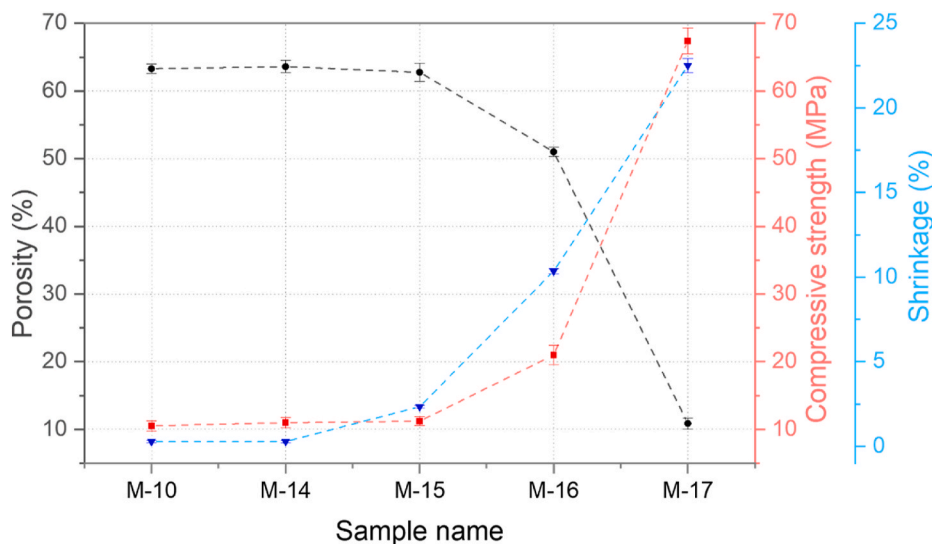

Fig. 7. Porosity, compressive strength, and shrinkage of porous mullite ceramics, which were prepared at several different temperatures: M-10 at 1000 °C, M-14 at 1400 °C, etc.
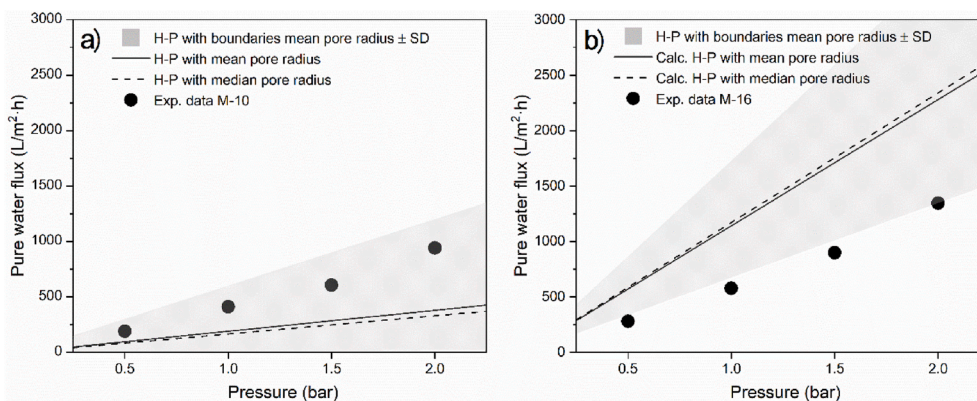
Fig. 8. Pure water flux of membranes M-10 (a) and M-16 (b) as a function of pressure. Dots represent experimental values, and the line/grey area show the values calculated according to the Hagen-Poiseuille (H–P) equation, eq. (6) (see text for the details). The mean and median pore radius were used to calculate the solid and dotted lines, respectively.

respect very close to an ideal tortuosity which is equal to unity. These values are comparable to those 1.12 and 1.16, which were recently reported for whisker-based mullite membranes [9,39]. These findings revealed that obtained mullite ceramics have high porosity and possess excellent connectivity of pores; both have paramount importance for the separation and filtration applications (i.e. permeance of membranes).

The pore size distribution of samples M-10 and M-16 are presented in Fig. 6. Sample M-10 exhibits a broader range of pores with a median diameter of 0.28 μm and bimodal pore size distribution. Also, the distribution of pore diameter skewed to the left, which means there are pores with pore diameter as small as 50 nm. This is because there are two possibilities for pores to form: i) interparticle pores are formed during the whisker formation; ii) replicate pores are formed after the decomposition of pore former/template. Here, $Al(OH)_3$ acts as a pore former because it undergoes 60 % volume contraction due to decomposition at high temperatures, which will produce extra porosity [40]. On the other hand, sample M-16 has a quite narrow pore size range with a larger median pore diameter of 0.78 μm compared to M-10. The larger and more uniform pore size distribution of M-16 can be attributed to pore widening and grain growth due to the coalescence of tiny particles into larger ones. At the same time, their number decreases during heating to high temperatures [40,41]. Hence, sample M-16 has larger pores with lower porosity relative to M-10.

3.4. The porosity and mechanical stability of mullite ceramics

Open porosities, diametral shrinkage, and compressive strengths of the sintered mullite ceramics are presented in Fig. 7. The samples M-10, M-14, and M-15, possess high porosities of about 63 ± 1 %, which can be explained by the evolution of fluoride-based gases, O_2, and water vapor during the synthesis process. Besides, as depicted in SEM images (Fig. 4), mullite whiskers grow as needle-like crystals, whereas their interlocked network produces a nest-like structure with high porosity [9]. At sintering temperatures higher than 1600 °C, the mullite approaches its melting point of about 1800 °C, and the densification of mullite is enhanced [42]. Thus, the porosity is remarkably decreased from 51 % to 11 % in the samples M-16 and M-17 sintered at 1600 °C and 1700 °C, respectively.

As known, the densification of porous bodies is accompanied by a decrease in their porosity and an increase in their mechanical strength [7]. Indeed, as displayed in Fig. 7, the shrinkage and compressive strengths of the samples are increased while their porosities are decreased. The similar porosity and mechanical stability of M-10, M-14, and M-15 suggest that the pore channels in mullite ceramics are stable up to 1500 °C, which might be promising for high-temperature applications, such as hot-gas filtration or thermal insulation. Since samples M-14 and M-15 do not show better mechanical strength than sample

M-10, the latter has been selected for permeance tests for economic reasons because it is prepared at a lower temperature. However, the sample M-16 still has adequate porosity and better mechanical stability than the sample M-10, which makes it very promising for filtration applications, where higher porosity with good mechanical strength is desired. In contrast, the sample M-17 has very low porosity despite its quite good mechanical stability, so it is not appropriate for filtration applications. Hence samples M-10 and M-16 were further investigated for their potential applications.

3.5. Water permeance test

As noted above, samples M-10 and M-16 have been chosen in this work for the water permeance tests. Pure water flux of samples was measured as described in the experimental section. Additionally, using all measured parameters porosity, pore size, and tortuosity, the pure water flux can be calculated according to the widely used Hagen-Poiseuille (H–P) equation [43]:

$$J_w = \frac{\varphi \cdot r^2 \cdot \Delta P}{8 \cdot \mu \cdot \tau \cdot \Delta x} \qquad (6)$$

where J_w is pure water flux (m/s or 1000 L/m²·h), φ is the porosity, r is the average pore radius (m), ΔP is the transmembrane pressure difference (Pa), μ is the viscosity of water (Pa·s), τ is the tortuosity of the membrane, and Δx is the thickness of the membrane (m). Fig. 8 displays the experimental water flux (data points) along with the values calculated (lines, a grey area considering the standard deviation) according to the eq. (6) from the available data (i.e. porosity, pore size distribution, tortuosity, membrane thickness, and pressure drop).

As shown in Fig. 8, the experimental water flux of the sample M-10 is within the calculated area (all dots are lying within the grey area), while the calculated and experimental water flux values of the sample M-16 are differing a lot (dots are lying out of the grey area). These results can be attributed to two reasons: First, the Hagen-Poiseuille equation, as well as the pore size distribution measurements using mercury porosimetry, assume the perfectly cylindrical shape of the pores. However, the porous mullite ceramics do not exhibit perfect cylindrical pores; instead, they are composed of an interlocked network of mullite whiskers, as shown in Fig. 4. This deviation from the cylindrical shape of the pores might cause this mismatch between the calculated and experimental water flux values. Secondly, not all of the open porosity determined by the Archimedes method might originate from through pores. Rather, also blind pores might contribute to the open porosity. However, as they are not of service for water permeation through the membrane, it can be assumed that the overall open porosity useful for permeation is lower than what was determined by the Archimedes method.

Table 2
Benchmarking of main properties of membranes with similar compositions.

Raw material	AlF$_3$ content, wt%	Processing temperature, °C	Porosity, %	Median Pore size, μm	Pure water flux at 1 bar, L/m^2·h	Reference
Kaolin, α-Al$_2$O$_3$ and AlF$_3$	40	1400	64	0.3	1031	[9]
Kaolin, α-Al$_2$O$_3$, Al(OH)$_3$, AlF$_3$	5	1500	46	1.3	4000	[36]
Kaolin, Al(OH)$_3$, AlF$_3$	NP[a]	1550	39	1.16	NA[a]	[18]
α-Al$_2$O$_3$-coated diaomite + kaolin	NA[a]	1200	NA[a]	0.12	200	[47]
α-Al$_2$O$_3$	NA[a]	1350	38	0.15	110	[48]
Kaolin, α-Al$_2$O$_3$	NA[a]	1350	56	NA[a]	582	[49]
Kaolin, α-Al$_2$O$_3$	NA[a]	1450	44	1.3	500	[50]
Metakaolin, Al(OH)$_3$, AlF$_3$	10	1000	63	0.28	479	This work
Metakaolin, Al(OH)$_3$, AlF$_3$	10	1600	51	0.78	576	This work

[a] NA – not applicable, NP- used but not presented.

Consequently, that led to a discrepancy between calculated and experimental flux values.

Besides, a higher flux (both experimental and calculated) is observed for the sample M-16 despite its lower porosity, i.e., the flux of the sample M-10 at 1 bar is 479 L/m^2·h, with 63 % porosity, but the flux of the sample M-16 at 1 bar is 576 L/m^2·h, with 51 % porosity. These results can also be due to the deviation from the cylindrical pore shapes and overestimation of porosity by Archimedes method, as explained above. Additionally, it appears that pore radius has a more significant impact on flux than porosity. Indeed, sample M-16 has larger pores with a median diameter of 0.78 μm, while sample M-10 has smaller pores with a median diameter of 0.28 μm.

The Hagen-Poiseuille equation appears to serve as a helpful instrument to obtain a first estimation of the pure water flux even for the presented whisker-based mullite ceramics. For more precise permeance calculations for fibrous porous media, other numerical approaches – such as the Carman-Kozeny model – have to be applied [44–46]. However, this would go beyond the scope of this study.

In Table 2, the main properties of ceramics fabricated in this work are compared with other membranes with similar compositions previously reported in the literature. Apparently, samples M-10 and M-16 show competitive porosity, pore size and permeance values.

Overall, experimental pure water flux results are quite promising, especially considering facile preparation, low-cost material metakaolin, and low-temperature processes (at least for M-10). The sample M-10 has high porosity with acceptable mechanical stability (withstanding against pressures as high as 2 bar in the water permeance experiments), making it suitable for applications where high mechanical strength is not required. Moreover, due to its high thermal stability and low thermal conduction of mullite, the sample M-10 can also be used directly in thermal insulation applications. However, if high mechanical strength is desired for water or hot-gas filtration applications, the sample M-16 sintered at 1600 °C could be promising.

4. Conclusions

In this work, the influence of aluminum sources, such as γ-Al(OH)$_3$, α-Al$_2$O$_3$, and AlF$_3$·3H$_2$O, on the crystallization temperature of mullite from metakaolin under fluoride-assisted condition has been investigated. The results of ex situ XRD, and in situ synchrotron XRD experiments revealed that γ-Al(OH)$_3$ led to the formation of phase pure mullite at temperature as low as 680 °C, while corundum α-Al$_2$O$_3$ did not react even at 1000 °C. SEM characterization showed that the mullite grew as needle-like whiskers. Moreover, the decomposition of Al(OH)$_3$ at high temperatures produces extra porosity, making this process attractive for membrane fabrication. Porous mullite ceramics were fabricated by preparing at several temperatures from 1000 °C to 1700 °C and tested for their applicability for water filtration. The results showed that interlocked mullite whiskers led to highly porous ceramics that presented competitive properties as a membrane with 0.78 μm median pore diameter, 51 % porosity, 20 MPa compressive strength, and 576 L/m^2·h at 1 bar pure water flux.

Conflicts of interest

The authors declare no conflict of interest.

CRediT authorship contribution statement

Amanmyrat Abdullayev: Conceptualization, Methodology, Investigation, Data curation, Writing – original draft, Preparation. **Celal Avcioglu:** Methodology, Investigation, Writing – review & editing. **Tobias Fey:** Investigation, Data curation. **André Hilger:** Investigation, Data curation. **Markus Osenberg:** Investigation, Data curation. **Ingo Manke:** Investigation, Data curation. **Laura M. Henning:** Methodology, Investigation, Formal analysis, Writing – review & editing. **Aleksander Gurlo:** Conceptualization, Supervision, Writing – review & editing, Project administration, Funding acquisition, Resources. **Maged F. Bekheet:** Conceptualization, Methodology, Investigation, Data curation, Writing – review & editing, Project administration, Supervision, All authors have read and agreed to the published version of the manuscript.

References

[1] R.P. Schwarzenbach, T. Egli, T.B. Hofstetter, U. von Gunten, B. Wehrli, Global water pollution and human health, Annu. Rev. Environ. Resour. 35 (2010) 109–136.

[2] Z. He, Z. Lyu, Q. Gu, L. Zhang, J. Wang, Ceramic-based membranes for water and wastewater treatment, Colloids Surf. A Physicochem. Eng. Asp. 578 (2019) 123513.

[3] E. Drioli, L. Giorno, E. Fontananova (Eds.), Comprehensive Membrane Science and Engineering, Elsevier, Amsterdam [the Netherlands], 2017.

[4] L. Sun, Z. Wang, B. Gao, Ceramic membranes originated from cost effective and abundant natural minerals and industrial wastes for broad applications - a review, DWT 201 (2020) 121–138.

[5] A. Abdullayev, M.F. Bekheet, D.A.H. Hanaor, A. Gurlo, Materials and applications for low-cost ceramic membranes, Membranes 9 (2019).

[6] H. Schneider, S. Komarneni, Mullite, Wiley-VCH, Chichester John Wiley [distributor], Weinheim, 2005.

[7] S. Komarneni, H. Schneider, K. Okada, in: H. Schneider, S. Komarneni (Eds.), Mullite Synthesis and Processing, Mullite, Wiley-VCH Verlag GmbH & Co. KGaA, Weinheim, FRG, 2005, pp. 251–348.

[8] M. Salleh Choo, Matori Kok, A review on synthesis of mullite ceramics from industrial wastes, Recycling 4 (2019) 39.

[9] M. Rashad, G. Logesh, U. Sabu, M. Balasubramanian, A novel monolithic mullite microfiltration membrane for oil-in-water emulsion separation, J. Membr. Sci. (2020), 118857.

[10] T.S. Zhang, L.B. Kong, Z.H. Du, J. Ma, S. Li, Tailoring the microstructure of mechanoactivated Al₂O₃ and SiO₂ mixtures with TiO₂ addition, J. Alloys Compd. 506 (2010) 777–783.

[11] J. She, P. Mechnich, M. Schmücker, H. Schneider, Low-temperature reaction-sintering of mullite ceramics with an Y₂O₃ addition, Ceram. Int. 27 (2001) 847–852.

[12] H. Ye, Y. Li, J. Sun, Y. Sun, X. Wu, M. Yan, Novel iron-rich mullite solid solution synthesis using fused-silica and α-Al₂O₃ powders, Ceram. Int. 45 (2019) 4680–4684.

[13] B. L″OCSEI, Mullite formation in the aluminium fluoride–silica system (AlF₃–SiO₂), Nature 190 (1961) 907–908.

[14] K. Okada, N. Otuska, Synthesis of mullite whiskers and their application in composites, J. Am. Ceram. Soc. 74 (1991) 2414–2418.

[15] M. Rashad, M. Balasubramanian, Characteristics of porous mullite developed from clay and AlF₃·3H₂O, J. Eur. Ceram. Soc. 38 (2018) 3673–3680.

[16] X. Deng, Y. Wu, T. Wei, S. Ran, L. Huang, H. Zhang, F. Li, L. Han, S. Ge, S. Zhang, Preparation of elongated mullite self-reinforced porous ceramics, Ceram. Int. 44 (2018) 7500–7508.

[17] A. Abdullayev, F. Zemke, A. Gurlo, M.F. Bekheet, Low-temperature fluoride-assisted synthesis of mullite whiskers, RSC Adv. 10 (2020) 31180–31186.

[18] G. Chen, H. Qi, W. Xing, N. Xu, Direct preparation of macroporous mullite supports for membranes by in situ reaction sintering, J. Membr. Sci. 318 (2008) 38–44.

[19] A. Doran, L. Schlicker, C.M. Beavers, S. Bhat, M.F. Bekheet, A. Gurlo, Compact low power infrared tube furnace for in situ X-ray powder diffraction, Rev. Sci. Instrum. 88 (2017) 13903.

[20] L. Schlicker, A. Doran, P. Schneppmüller, A. Gili, M. Czasny, S. Penner, A. Gurlo, Transmission in situ and operando high temperature X-ray powder diffraction in variable gaseous environments, Rev. Sci. Instrum. 89 (2018) 33904.

[21] B.A. Dowd, G.H. Campbell, R.B. Marr, V.V. Nagarkar, S.V. Tipnis, L. Axe, D. P. Siddons, Developments in synchrotron X-ray computed microtomography at the national synchrotron Light source, in: U. Bonse (Ed.), Developments in X-Ray Tomography II, SPIE, 1999, pp. 224–236.

[22] D. Legland, I. Arganda-Carreras, P. Andrey, MorphoLibJ: integrated library and plugins for mathematical morphology with ImageJ, Bioinformatics 32 (2016) 3532–3534.

[23] C21 Committee, Test Methods for Determination of Water Absorption and Associated Properties by Vacuum Method for Pressed Ceramic Tiles and Glass Tiles and Boil Method for Extruded Ceramic Tiles and Non-tile Fired Ceramic Whiteware Products, ASTM International, West Conshohocken, PA.

[24] E.W. Washburn, The dynamics of capillary flow, Phys. Rev. 17 (1921) 273–283.

[25] R.V. Kumar, A.K. Basumatary, A.K. Ghoshal, G. Pugazhenthi, Performance assessment of an analcime-C zeolite–ceramic composite membrane by removal of Cr(vi) from aqueous solution, RSC Adv. 5 (2015) 6246–6254.

[26] M. Rashad, M. Balasubramanian, A quantitative analysis of in-situ gases on the properties of porous mullite developed from clay and AlF₃·3H₂O, Ceram. Int. 45 (2019) 1420–1423.

[27] X. Delong, L. Yongqin, J. Ying, Z. Longbao, G. Wenkui, Thermal behavior of aluminum fluoride trihydrate, Thermochim. Acta 352–353 (2000) 47–52.

[28] P.S. Santos, H.S. Santos, S.P. Toledo, Standard transition aluminas. Electron microscopy studies, Math. Res. 3 (2000) 104–114.

[29] I. Levin, D. Brandon, Metastable Alumina polymorphs: crystal structures and transition sequences, J. Am. Ceram. Soc. 81 (1998) 1995–2012.

[30] B.R. Cho, J.B. Kang, Synthesis of porous mullite by vapor phase reaction, MSF 449–452 (2004) 209–212.

[31] J.R. Moyer, N.N. Hughes, A catalytic process for mullite whiskers, J. Am. Ceram. Soc. 77 (1994) 1083–1086.

[32] J.R. Moyer, P.R. Rudolf, Stoichiometry of fluorotopaz and of mullite made from fluorotopaz, J. Am. Ceram. Soc. 77 (1994) 1087–1089.

[33] D. XIE, L. Yang, L. Li, W. Wang, J. Liu, H. DU, X. Hu, The formation mechanism of mullite whisker in the mullite fiber network, J. Ceram. Soc. Japan 126 (2018) 529–535.

[34] M. Rashad, U. Sabu, G. Logesh, C. Srishilan, M. Lodhe, A. Joy, M. Balasubramanian, Mullite phase evolution in clay with hydrated or anhydrous AlF3, J. Eur. Ceram. Soc. 40 (2020) 5974–5983.

[35] M. Rashad, U. Sabu, G. Logesh, M. Balasubramanian, Development of porous mullite and mullite-Al2O3 composite for microfiltration membrane applications, Separ. Purif. Technol. 219 (2019) 74–81.

[36] G. Chen, X. Ge, Y. Wang, W. Xing, Y. Guo, Design and preparation of high permeability porous mullite support for membranes by in-situ reaction, Ceram. Int. 41 (2015) 8282–8287.

[37] X. Deng, S. Ran, L. Han, H. Zhang, S. Ge, S. Zhang, Foam-gelcasting preparation of high-strength self-reinforced porous mullite ceramics, J. Eur. Ceram. Soc. 37 (2017) 4059–4066.

[38] A.J. Pyzik, C.S. Todd, C. Han, Formation mechanism and microstructure development in acicular mullite ceramics fabricated by controlled decomposition of fluorotopaz, J. Eur. Ceram. Soc. 28 (2008) 383–391.

[39] Li Zhu, Y. Dong, S. Hampshire, S. Cerneaux, L. Winnubst, Waste-to-resource preparation of a porous ceramic membrane support featuring elongated mullite whiskers with enhanced porosity and permeance, J. Eur. Ceram. Soc. 35 (2015) 711–721.

[40] R. Ahmad, J.-H. Ha, I.-H. Song, Synthesis of open-cell particle-stabilized Al₂O₃ foam using Al(OH)₃ particles, Scripta Mater. 76 (2014) 85–88.

[41] J.A. Varela, O.J. Whittemore, E. Longo, Pore size evolution during sintering of ceramic oxides, Ceram. Int. 16 (1990) 177–189.

[42] H. Schneider, J. Schreuer, B. Hildmann, Structure and properties of mullite—a review, J. Eur. Ceram. Soc. 28 (2008) 329–344.

[43] M. Mulder, in: Basic Principles of Membrane Technology, second ed., Kluwer Acad. Publ, Dordrecht, 1996 [u.a.].

[44] B. Xiao, W. Wang, X. Zhang, G. Long, J. Fan, H. Chen, L. Deng, A novel fractal solution for permeability and Kozeny-Carman constant of fibrous porous media made up of solid particles and porous fibers, Powder Technol. 349 (2019) 92–98.

[45] T.J. Donohue, C.M. Wensrich, Improving permeability prediction for fibrous materials through a numerical investigation into pore size and pore connectivity, Powder Technol. 195 (2009) 57–62.

[46] J. Cai, L. Luo, R.A. Ye, X. Zeng, X. Hu, Recent advances on fractal modeling of permeability for fibrous porous media, Fractals 23 (2015), 1540006.

[47] J.-H. Ha, S.Z. Abbas Bukhari, J. Lee, I.-H. Song, C. Park, Preparation processes and characterizations of alumina-coated alumina support layers and alumina-coated natural material-based support layers for microfiltration, Ceram. Int. 42 (2016) 13796–13804.

[48] N. Das, S. Bandyopadhyay, D. Chattopadhyay, H.S. Maiti, Tape-cast ceramic membranes for microfiltration application, J. Mater. Sci. 31 (1996) 5221–5225.

[49] M. Abbasi, M. Mirfendereski, M. Nikbakht, M. Golshenas, T. Mohammadi, Performance study of mullite and mullite–alumina ceramic MF membranes for oily wastewaters treatment, Desalination 259 (2010) 169–178.

[50] S. Sarkar, S. Bandyopadhyay, A. Larbot, S. Cerneaux, New clay–alumina porous capillary supports for filtration application, J. Membr. Sci. 392–393 (2012) 130–136.